applied sciences

MDPI

Article

Research on Damage Identification of Suspension Bridges Based on Visual Image Recognition Technology

Xingshun Liu and Kun Ma *

Faculty of Civil Engineering and Mechanics, Kunming University of Science and Technology, Kunming 650500, China; liuxingshun@stu.kust.edu.cn
* Correspondence: 11305063@kust.edu.cn

Abstract

To address the challenge of identifying damage in the hangers and bridge deck systems of long-span suspension bridges, this paper proposes a non-contact monitoring method based on video image recognition. This method extracts structural vibration displacement responses through video acquisition and image analysis, and combined with the strain mode change rate index, it achieves damage localization, type identification, and severity assessment. The principle of extracting displacement time-history data from video images is first elaborated, and MATLAB-based computational code is developed, including pixel tracking and time-history curve generation methods. The eigensystem realization algorithm is used to identify displacement mode shapes, which are then converted into strain mode shapes via the central difference method. The strain mode change rate and its deviation rate are proposed as damage indicators: under undamaged conditions, the curve is smooth; at damage locations, peaks appear; the distribution range of peaks can distinguish between hanger damage and bridge deck cracks; the deviation rate quantifies damage severity. The feasibility of the method is validated through finite element simulations and physical model experiments. The results show that hanger damage causes broad peaks, while bridge deck cracks present narrow peaks; the deviation rate increases monotonically with damage severity. Applied to an in-service suspension bridge, the method successfully identified hanger bending and weld cracking, with assessment results consistent with on-site inspections. This study demonstrates that the strain mode change rate analysis based on video images enables damage identification without prior knowledge of the structural health state, relying solely on the damaged state response. Offering advantages such as non-contact measurement, full-field monitoring, and no need for sensor deployment, it provides a new technical approach for the long-term monitoring of suspension bridge hanger systems.

Keywords: suspension bridge; finite element analysis; image recognition; testing and analysis; damage identification; health monitoring; strain mode change rate

Check for updates

Academic Editor: Pedro Couto

Received: 24 January 2026
Revised: 25 February 2026
Accepted: 4 March 2026
Published: 6 March 2026

1. Introduction

With the advancement of infrastructure construction into remote areas characterized by complex terrain, long-span suspension bridges have become a critical engineering solution [1,2]. However, the hanger system, as a key force-transmitting component, has a relatively short development history, and the understanding of its long-term service performance and damage mechanisms remains insufficient, posing a potential risk to the long-term safety of suspension bridges [3–6].

Structural damage identification is fundamentally a pattern recognition problem [7,8]. It involves extracting damage-sensitive features (such as modal parameters and wavelet features) from structural response signals [9,10] and utilizing neural networks, support vector machines, or evolutionary algorithms to establish mapping relationships between these features and damage parameters (location, severity) for predictive purposes [11,12].

The development of the Internet of Things and advanced sensor technologies has provided the hardware foundation for achieving massive and real-time monitoring of cable forces and vibrations [13–17]. However, building an effective intelligent monitoring system requires the deep integration of precise mechanical models, optimized sensor networks, and advanced data processing algorithms [18–22]. Research cases have demonstrated the feasibility of this approach, such as combining modal flexibility with genetic algorithms [23], wavelet features with neural networks [24], and employing a two-stage strategy integrating support vector machines and evolutionary algorithms [25], among others.

Current research frontiers focus on the integration of artificial intelligence, big data, and cloud computing to develop real-time assessment and early warning systems [26–29]. Simultaneously, monitoring the static and dynamic response distribution under operational loads provides an important pathway for identifying abnormalities in hanger cable forces or local stiffness loss [30–33]. In contrast, traditional cable force measurement methods, such as frequency-based approaches, are limited by factors such as bending stiffness and boundary conditions, resulting in insufficient accuracy and long-term online monitoring capabilities [34–37].

The hanger system itself faces severe service challenges. It operates under long-term high-stress conditions and is exposed to corrosive environments. The protective layers are prone to aging and failure [38,39], and steel wires may experience stress corrosion and fatigue. Additionally, the concealed anchoring system poses a high risk of damage [40–42]. These types of damage are interconnected and may lead to progressive deterioration or even sudden fracture. Although the design life typically requires no less than 20 years [43], actual cyclic loading can accelerate degradation [44–46]. Damage to a single hanger can alter the overall cable force distribution, affect the stress on the stiffening girder, and in extreme cases, may lead to cascading failures or even structural collapse [47–50].

Therefore, developing a new generation of intelligent damage identification methods that combine cross-disciplinary information fusion and data-driven approaches, and constructing a full-life-cycle intelligent health monitoring system, holds strategic significance for ensuring the long-term safe operation of suspension bridges. This study proposes a method for damage identification in suspension bridges using image recognition technology. Through video image analysis and validation against finite element simulation results, the strain mode change rate is extracted as a damage indicator. The method is further verified through a real bridge case study, with the results aligning well with actual conditions. Figure 1 illustrates the flowchart of the damage identification analysis for suspension bridges based on video image recognition technology.

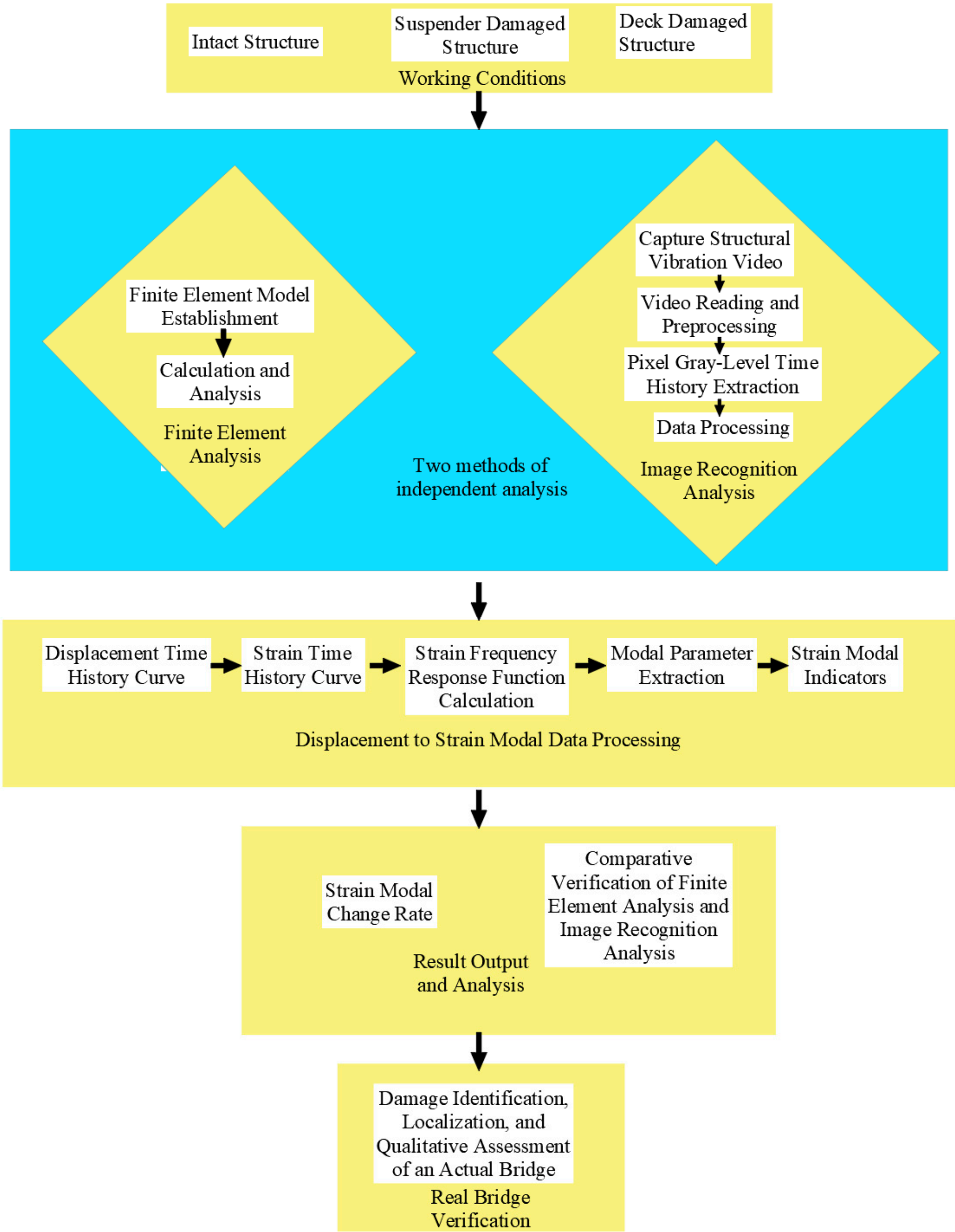

Figure 1. Flowchart of damage identification analysis for suspension bridges based on video image recognition technology.

2. Theoretical Analysis

2.1. Image Processing and Phase Correlation

2.1.1. Video Acquisition

Video capture is performed using a camera with a frame rate of no less than 30 fps and a resolution of no lower than 1080 p. Recordings should be conducted under stable temperature conditions and windless weather to minimize environmental interference. During acquisition, the camera must be positioned directly facing the bridge, with an angular deviation not exceeding 30 degrees. The shooting distance should be adjusted to ensure the entire bridge structure is within the image frame. The camera must remain stable throughout the process, and the duration of each recording should be no less than three minutes.

2.1.2. Video Frame Reading and Implementation

Video frames are read sequentially, based on stream reading and internal pointer management. Each call to the reading function returns the video frame at the current pointer position and automatically advances the internal pointer to the next frame. The frame data is returned as a three-dimensional array. The computation can be implemented using operational code developed based on MATLAB R2021a's VideoReader (subsequent code will not be listed in detail; see Supplementary Materials, Code S1). The operational code is as follows:

```
% readFrame() has implicit pointer movement logic
v = VideoReader('video.mp4');
% First call: read frame 1, pointer moves to position of frame 2
frame1 = readFrame(v); % ← Pointer position: 1→2
% Second call: read frame 2, pointer moves to position of frame 3
frame2 = readFrame(v); % ← Pointer position: 2→3
% Determine if there are subsequent frames
while hasFrame(v) % ← Check if pointer position is valid
frame = readFrame(v);
% Process frame data
end
```

2.1.3. Pixel Tracking

The scale factor, which converts pixel displacements to physical units (millimeters or meters), was determined through geometric calibration using an object of known dimensions within the camera's field of view. The specific procedure is as follows: Laboratory Setup: In the laboratory experiments, a calibration object (e.g., a ruler with known grid spacing) was placed at the same distance from the camera as the bridge model. The scale factor was determined by identifying two points with a known physical distance in the image and calculating the number of pixels between them. To achieve sub-pixel accuracy, the peak in the correlation plane is localized using 2D Gaussian fitting, enabling displacement measurements with a precision of 0.01 pixels. In a video sequence, the brightness value of each pixel point (x, y) changes over time and can be expressed as [51]

$$I(x,\ y,\ t) = I_0(x,\ y) + f(t) \cdot B(x,\ y) + noise, \tag{1}$$

where $I^0(x,\ y)$: static background brightness

$$f(t) : \text{time} - \text{varying function}$$
$$B(x,\ y) : \text{brightness variation pattern related to motion.}$$

Phase change detection is employed, as phase variations directly correspond to object motion [52]:

$$\varphi(x,\ y,\ t)\ =\ \omega t\ +\ \varphi_0(x\ +\ \delta(t)), \tag{2}$$

where ω : Spatial frequency

$$\delta(t) : \text{Time} - \text{varying displacement}$$
$$\text{Phase change } \Delta\varphi \text{ directly corresponds to displacement } \Delta x.$$

The Phase Correlation Method is a frequency-domain image registration technique used to accurately calculate translational relationships between two images. The core principle is that translational differences in the spatial domain manifest as phase differences in the frequency domain. For a two-dimensional image $f(x, y)$, its Fourier transform is $F(u, v)$ [53]. If the image undergoes translation $(\Delta x, \Delta y)$:

$$f_2(x, y) = f_1(x - \Delta x, y - \Delta y), \tag{3}$$

where

$f_1(x, y)$: Pixel value of the reference image (the first image) at spatial coordinates (x, y)
$f_2(x, y)$: Pixel value of the target image (the second image) at spatial coordinates (x, y)
x, y: Spatial coordinates, representing the position of image pixels (unit: pixels)
Δx: Horizontal translation amount (displacement in the x-direction, unit: pixels)
Δy: Vertical translation amount (displacement in the y-direction, unit: pixels)
Physical meaning: The target image f_2 is the result of translating the reference image f_1 by Δx in the x-direction and Δy in the y-direction [54].

According to the Fourier shift theorem:

$$F_2(u, v) = F_1(u, v) \cdot e^{(-j2\pi(u\Delta x + v\Delta y))}, \tag{4}$$

where

$$F_1(u, v) : \text{Two} - \text{dimensional Fourier transform of the reference image } f_1(x, y)$$

$$F_2(u, v) : \text{Two} - \text{dimensional Fourier transform of the target image} f_2(x, y)$$

$$u, v : \text{Frequency coordinates (unit : cycles per pixel)}$$

$$u : \text{Horizontal frequency component}$$

$$v : \text{Vertical frequency component}$$

$$j : \text{Imaginary unit, } j^2 = -1$$

$$\pi : \text{Pi, approximately 3.14159}$$

$$exp() : \text{Exponential function,} exp(z) = e^z, \text{ where e is the base of the natural logarithm}$$

$$2\pi(u\Delta x + v\Delta y) : \text{Phase change amount (unit : radians)}$$

Physical meaning: Translation in the spatial domain results in a linear phase change in the frequency domain.

It can be observed that translation affects only the phase and not the amplitude spectrum [55,56]. The phase difference is given by

$$F_2(u, v) = F_1(u, v) \cdot e^{(-j\varphi(u, v))}, \tag{5}$$

where

$\varphi(u, v)$: Phase difference function, representing the phase difference between the two images at frequency (u, v)
$-j\varphi(u, v)$: Phase part of the complex exponential, with the negative sign indicating phase delay

The specific form is

$$\varphi(u, v) = 2\pi(u\Delta x + v\Delta y), \tag{6}$$

where

$\varphi(u, v)$: Linear phase function
$u\Delta x$: Phase contribution of horizontal displacement Δx at frequency u

$v\Delta y$: Phase contribution of vertical displacement Δy at frequency v
2π: Conversion factor from cycles to radians

Physical meaning: The phase difference caused by translation is linearly related to frequency.

The normalized cross-power spectrum is defined as:

$$R(u,\ v)\ =\ \frac{F_1(u,\ v)\cdot F_2*(u,v)}{|F_1(u,\ v)\cdot F_2*(u,\ v)|}/\ =\ e^{(j\varphi(u,\ v))}, \tag{7}$$

where

$R(u, v)$: Normalized cross-power spectrum
F_2*(u, v): Complex conjugate of $F_2(u, v)$ (imaginary part negated)
$|\cdot|$: Magnitude (amplitude) of a complex number, $|a + jb| = \sqrt{(a^2 + b^2)}$
$F_1(u, v) \cdot F_2$*(u, v): Cross-power spectrum (unnormalized)
$/|F_1(u, v) \cdot F_2$*$(u, v)|$: Normalization operation, ensuring the magnitude is 1
$exp(j\varphi(u, v))$: Pure phase signal with magnitude 1 and phase $\varphi(u, v)$

Complex conjugate multiplication: $F_1 \cdot F_2$* yields phase difference information. Magnitude normalization: Removes amplitude information, retaining only pure phase information. Substituting the translation relationship:

$$R(u,\ v)\ =\ e^{(j2\pi(u\Delta x\ +\ v\Delta y))}, \tag{8}$$

Perform an inverse Fourier transform on the cross-power spectrum:

$$r(x,\ y)\ =\ F^{-1}\{R(u,\ v)\}\ =\ \delta(x\ -\ \Delta x,\ y\ -\ \Delta y), \tag{9}$$

where

$r(x, y)$: Correlation plane (result of cross-correlation in the spatial domain)
$F^{-1}\{\cdot\}$: Two-dimensional inverse Fourier transform, transforming from the frequency domain back to the spatial domain
$\Delta(x, y)$: Two-dimensional Dirac delta function (impulse function)
$\Delta(x - \Delta x, y - \Delta y)$: Translated impulse function

A Dirac delta function is obtained, and the peak position corresponds to the translation amount $(\Delta x, \Delta y)$. The above calculations can be implemented using code developed with MATLAB EVM (see Supplementary Materials, Code S2. Pixel Tracking).

2.1.4. Displacement Time-History Curve

By analyzing the frame-by-frame translation of a given point, its displacement time-history curve and data can be obtained. This is implemented using MATLAB EVM (see Supplementary Materials: Code S3. Displacement Time-History Data).

2.1.5. Data Denoising and Smoothing

In vibration signal processing, filtering and smoothing are two essential preprocessing techniques used to enhance signal quality and provide reliable inputs for subsequent modal analysis.

The primary purpose of filtering is to remove noise components from the signal while retaining the frequency components of interest. The code employs two filtering techniques. Butterworth Low-Pass Filter: This filter features a maximally flat magnitude response in the passband, effectively preserving low-frequency signal components while suppressing high-frequency noise. A 4th-order Butterworth filter is used, with the cutoff frequency adaptively determined based on signal characteristics. Zero-Phase Digital Filtering: Implemented via the filtfilt function, this technique filters the signal in both forward and reverse directions, effectively eliminating phase distortion. This is particularly critical for vibration analysis, as phase information directly impacts the accuracy of modal parameter identification.

Smoothing aims to reduce local fluctuations in the data, resulting in a smoother curve that facilitates trend observation and feature extraction. The code utilizes:Moving Average Filter: Implemented via the smooth function, it averages each data point with its neighboring points (using a window size of 5). This process suppresses the high-frequency noise amplified by numerical differentiation (e.g., during velocity and acceleration calculations), leading to more stable and reliable dynamic response curves.

2.2. Modal Identification

2.2.1. Constructing the Hankel Matrix

To identify the modal parameters of the structure from the displacement response data, the time-history data must first be reconstructed into a specific matrix form. In the stochastic subspace identification method, the construction of the Hankel matrix is a fundamental step for achieving modal identification—it rearranges the displacement response data, which contains both spatial and temporal information, into a block Toeplitz form suitable for subsequent orthogonal projection and matrix decomposition. The Hankel matrix $\boldsymbol{H}(0)$ (i.e., the case for $k = 1$) constructed based on Equation (10) essentially establishes the statistical relationship between the "past" input and the "future" response, thereby providing the necessary data organization format for extracting displacement mode shapes using the Eigensystem Realization Algorithm in Section 2.2.2.

From the displacement time-history data of mm measurement points $ui(k)$(where $I = 1, 2, \ldots, mi = 1, 2, \ldots, m$ and $k = 1, 2, \ldots, Nt$ represents the discrete time point indices), construct the following [57,58]:

$$H(k-1) = \begin{bmatrix} u(k) & \ldots & u(k+s-1) \\ \vdots & \ddots & \vdots \\ u(k+r-1) & \ldots & u(k+r+s-2) \end{bmatrix}, \tag{10}$$

where

$u(k)$: an $m \times 1$ column vector composed of the displacements of all measurement points at time point k,$u(k) = [u_1(k), u_2(k), u_m(k)]^T$

r,s: selected block dimensions of the Hankel matrix (positive integers). The block row count of matrix H is r, and the block column count is s, with its dimension being $(r \cdot m) \times s$.

N: the expected system state-space model order (twice the number of modes to be identified)

$H(k-1)$: the Hankel matrix constructed starting from time index k. In particular, $H(0)$ is often referred to as the "future-past" matrix or the matrix directly used for decomposition

Rule: Typically, $r \cdot m \geq 2N$ is chosen to ensure the identification of an N-order system. The computation can be implemented using operational code developed based on MATLAB (see Supplementary Materials: Code S4. Hankel Matrix).

2.2.2. Singular Value Decomposition (SVD)

Perform singular value decomposition on the initial Hankel matrix H(0) to determine the effective system order [59].

$$H(0) = U\Sigma V^T, \tag{11}$$

where

U: Left singular vector matrix, with orthogonal column vectors.

Σ: Singular value matrix, a diagonal matrix $diag(\sigma 1, \sigma 2, \ldots, \sigma min(rm,s))$, with $\sigma 1 \geq \sigma 2 \geq \cdots \geq 0$
V: Right singular vector matrix, with orthogonal column vectors.
Un, Σn, Vn: Truncated matrices corresponding to the first nn significant singular values and their associated left and right singular vectors, where $\Sigma n = diag(\sigma 1, \sigma 2, \ldots, \sigma n)$

The computation can be implemented using code developed based on MATLAB (see Supplementary Materials: Code S5. Singular Value Decomposition (SVD)).

2.2.3. Extracting System Matrices

Using the results of the Singular Value Decomposition (SVD) and the time-shift relationship of the Hankel matrix, the system matrices of the discrete-time state-space model are extracted [57,60,61]. Define the selection matrix:

$$E_m^T = [I_m \; 0 \; \cdots \; 0], \tag{12}$$

where

I_m: An $m \times m$ identity matrix
E_m^T: An $m \times (r{\cdot}m)$ matrix used to select the first m rows (i.e., the response of the first time block) from a block matrix.

The discrete-time system matrices A_d and the output matrix C are calculated as follows:

$$\begin{gathered} A_d = \Sigma_n^{-\frac{1}{2}} U_n^T H(1) V_n \Sigma_n^{-\frac{1}{2}} \\ C = E_m^T U_n \Sigma_n^{\frac{1}{2}}, \end{gathered} \tag{13}$$

where

$H(1)$: The Hankel matrix shifted one step forward in time, i.e., constructed starting from $k = 2$
A_d: The discrete-time n $\times$ n state matrix, describing the evolution of the system state over the sampling interval Δt.
C: The discrete-time m $\times$ n output matrix, describing how the system state is mapped to the observed displacement outputs.
$\Sigma_n^{-\frac{1}{2}}$: The negative square root of the diagonal matrix Σ_n, i.e., $diag(1/\sqrt{\sigma_1}, \ldots, 1/\sqrt{\sigma_n})$
$\Sigma_n^{\frac{1}{2}}$: The square root of the diagonal matrix Σ_n, i.e., $diag(\sqrt{\sigma_1}, \ldots, \sqrt{\sigma_n})$

The computation can be implemented using code developed based on MATLAB (see Supplementary Materials: Code S6. Extracting System Matrices).

2.2.4. Modal Parameter Identification

Perform eigenvalue analysis on the extracted discrete-time system matrix to convert it into continuous-time modal parameters [62,63].
Step 1: Eigenvalue decomposition of A_d:

$$A_d \Psi = \Psi \Lambda_d, \tag{14}$$

where

Ψ: an $n \times n$ matrix whose column vectors ψ_i are the eigenvectors of the discrete-time state matrix A_d
Λ_d: a diagonal matrix $diag(\mu_1, \mu_2, \ldots, \mu_n)$), where μ_i are the discrete-time eigenvalues (complex numbers).

Step 2: transformation to the continuous-time domain

The relationship between the continuous-time eigenvalue λ_i and the discrete-time eigenvalue μ_i is:

$$\lambda_i = \frac{ln(\mu_i)}{\Delta t}, \tag{15}$$

where

λ_i: the continuous-time eigenvalue (complex) of the *i-th* mode.
Δt: data sampling time interval.
$ln(\cdot)$: natural logarithm of a complex number.

Step 3: Calculation of natural frequency and damping ratio

Compute physical modal parameters from the continuous-time eigenvalues λ_i:

$$\omega_{ni} = \mid \lambda_i \mid, \zeta_i = -\frac{Re(\lambda_i)}{\mid \lambda_i \mid}, \tag{16}$$

where

$\omega_n i$: the (undamped) natural circular frequency (rad/s) of the *i-th* mode.
ζ_i: the damping ratio of the *i-th* mode.
$/\cdot/$: modulus of a complex number.
$Re(\cdot)$: real part of a complex number.

Step 4: Calculation of displacement mode shapes

Obtain the displacement mode shapes at observation points (measurement points) via the output matrix C and the state eigenvectors Ψ:

$$\{\phi_u\}_i = C\psi_i, \tag{17}$$

where

$\{\phi_u\}_i$: an $m \times 1$ complex column vector representing the displacement mode shape of the *i-th* mode across the m measurement points. Typically, its amplitude and phase information are used, or only its real or imaginary part is taken (for proportionally damped systems, mode shapes are real vectors).
ψ_i: the *i-th* column of matrix Ψ, i.e., the discrete-time state eigenvector corresponding to eigenvalue μ_i (and λ_i).

The computation can be implemented using code developed based on MATLAB (see Supplementary Materials: Code S7. Modal Parameter Identification).

2.2.5. Identifying Displacement Mode Shapes from Displacement Time-History Curves

Its elements correspond to the relative displacement amplitudes at each measurement point. The measurement points are evenly spaced along the length direction of the beam (x-axis) with a spacing of Δx. For the i-th internal measurement point (i.e., not at the boundary endpoints), the strain mode shape value can be approximated by calculating the spatial second derivative (curvature) of the displacement mode shape [64,65]:

$$\phi_\varepsilon(x_i) = -y \cdot \frac{\partial^2 \phi_u(x)}{\partial x^2}\bigg|_{x=x_i} \approx -y \cdot \frac{\phi_u(x_{i-1}) - 2\phi_u(x_i) + \phi_u(x_{i+1})}{(\Delta x)^2}, \tag{18}$$

where

$\phi_\varepsilon(x_i)$: the *n-th* strain mode shape value calculated at the *i-th* measurement point x_i. It is a complex (or real, depending on damping type) number representing the relative strain amplitude and phase of this mode at the point

y: The vertical distance from the measurement point to the neutral axis of the beam. This is a key geometric parameter. For surface strain measurement: If strain gauges or sensors are attached to the beam's surface, then $y = h/2$, where h is the thickness (or height) of the beam cross-section. Sign explanation: The negative sign "-" in the formula originates from the convention in beam bending theory relating curvature and bending moment (positive bending moment causes compressive strain on the upper surface when downward deflection is positive)

$\frac{\partial^2 \phi_u(x)}{\partial x^2}$: The second derivative of the displacement mode shape function $\phi_u(x)$ with respect to the spatial coordinate x, which physically represents the modal curvature in beam theory

$\phi_u(x_{i-1}), 2\phi_u(x_i), \phi_u(x_{i+1})$:The *n-th* displacement mode shape values at three adjacent measurement points x_{i-1},x_i,x_{i+1}. These values are taken from the known displacement mode shape vector $\{\phi_u\}_{\mathrm{n}}$

Δx: The spatial interval between adjacent measurement points (units consistent with length units, e.g., meters). The measurement points must be uniformly distributed along the beam axis.

$\frac{\phi_u(x_{i-1}) - 2\phi_u(x_i) + \phi_u(x_{i+1})}{(\Delta x)^2}$: Discrete numerical approximation of the second derivative $\frac{\partial^2 \phi_u}{\partial x^2}$ using the central difference method. This formula applies only to internal measurement points.

The computation can be implemented using code developed based on MATLAB (see Supplementary Materials: Code S8. From Displacement Mode to Strain Mode).

2.3. Strain Mode Change Rate and Deviation Rate of Strain Mode Change Rate

2.3.1. Strain Mode Change Rate

The strain mode change rate is defined as the first-order derivative of the strain mode shape after damage. Its calculation formula is [66]:

$$\phi'_\varepsilon(x_i) = \frac{\phi_\varepsilon(x_{i+1}) - \phi_\varepsilon(x_i)}{l_p}, \tag{19}$$

where

$\phi_\varepsilon(x_i)$: the *n-th* strain mode shape value calculated at the *i-th* measurement point x_i.

l_p: The distance between the *i-th* and *(i + 1)-th* nodes.

2.3.2. Deviation Rate of Strain Mode Change Rate

Spatially, strain values on either side of a damage location exhibit significant differences. This discontinuity results in an abrupt change in the first derivative (slope) of strain with respect to location and a sharp peak in the second derivative (curvature), approaching a singularity in ideal terms but manifesting as a distinct peak in measured data. In contrast, an undamaged structure produces a smooth strain mode change rate curve.

A smooth curve representing the undamaged condition can be fitted to the strain mode change rate data of the damaged structure. The smooth reference curve representing the undamaged condition was obtained using a robust LOESS (Locally Estimated Scatterplot Smoothing) filter with a span of 0.3 and linear local polynomials. The robust version employs iterative reweighting using a bisquare function to down-weight the influence of damage-induced peaks, ensuring that the fitted curve provides an unbiased baseline for the deviation rate calculation. Four robust iterations were performed to achieve stable convergence. The deviation rate is then defined as the normalized difference between the peak value at the damage location and the corresponding value on this fitted curve:

$$\lambda = \frac{\phi'_\varepsilon(x_i) - \widetilde{\phi'_\varepsilon(x_i)}}{\widetilde{\phi'_\varepsilon(x_i)}}, \tag{20}$$

where

λ: deviation rate of the strain mode change rate.
$\phi'_{\varepsilon}(x_i)$: strain mode change rate at the damage location.
$\widetilde{\phi'_{\varepsilon}(x_i)}$: strain mode change rate at the corresponding location on the fitted curve.

2.4. Summary

The essence of structural damage lies in material or connection failure, leading to a reduction in the elastic modulus EE or the moment of inertia II of the damaged area, i.e., a decrease in local stiffness. Under the same load or vibrational excitation, regions with lower stiffness will experience larger strains to coordinate the overall deformation. This results in an increase in the amplitude of the strain mode at the damage location.

(1) Displacement time-history data at corresponding points can be extracted from vibration videos of the structure.
(2) From the displacement time-history data at these points, the strain mode, strain mode change rate, and deviation rate of the strain mode change rate can be derived.
(3) The damage location can be identified based on the position of the sharp peak.
(4) The type and severity of damage can be assessed based on the shape of the sharp peak and the deviation rate of the strain mode change rate.

3. Damage Identification Analysis Based on Strain Mode Change Rate and Its Deviation Rate

3.1. Physical Model

3.1.1. Structural Parameters

The bridge model has a span of 8.25 m, with a main cable spacing of 300 mm and hanger spacing of 0.4 m. The numbering of the hangers is shown in Figure 2. The main cable follows a parabolic profile. In the coordinate system established in Figure 2, the origin is located at the mid-span of the main cable, and the parabolic equation is given by $y = 0.000045583x^2$ (units: mm). The main cable is made of high-strength steel wires with a diameter of 6 mm and an elastic modulus of 120 GPa. The hangers are steel rods with a diameter of 6 mm (featuring surface threads) and are made of Q235 steel. The bridge deck is a steel plate with a width of 400 mm and a thickness of 2.5 mm, also made of Q235 steel.

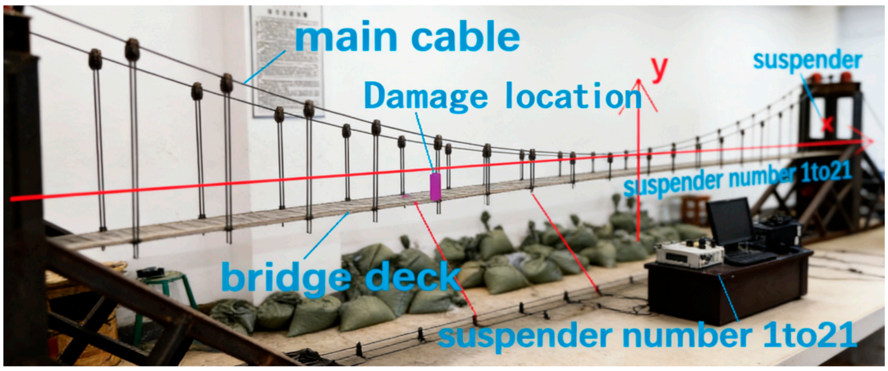

Figure 2. Physical Model Diagram.

3.1.2. Load Cases

This analysis employs a cosine load to simulate moving loads on the bridge deck, aiming to investigate the influence of moving and varying loads on the stress in adjacent hangers. The moving path of the load spans longitudinally from one side of the bridge to the other, and its expression is as follows:

$$F(t) = Q + P \cdot cos(2\pi f_s t), \tag{21}$$

where

$F(t)$: vertical time-history load (unit: N).
Q: self-weight.
P: load peak value.
f_s: frequency (unit: Hz).
t: time (unit: s).

To analyze the impact under different working conditions, multiple groups of comparative load cases were set by changing the frequency, peak value and moving speed of the load. The specific load conditions are detailed in Table 1:

Table 1. Load Condition Table.

Load Conditions	Frequency (f_s)	Load Peak Value (P)	Speed
	Hz	N	m/s
A	1	40	0.5
B	1	60	0.5

3.1.3. Damage Cases

To investigate the variation patterns of the structural strain mode change rate under different damage conditions, damage cases were introduced at the quarter-span position of the bridge. In the experimental analysis, hanger damage was simulated as a reduction in the effective cross-sectional area, while deck damage was simulated as physical cracking. In the finite element analysis, hanger damage was modeled as a reduction in cross-sectional area, and deck damage was modeled as a reduction in elastic modulus. The specific damage cases are detailed in Table 2:

Table 2. Damage Case Table.

Working Condition	Damage Location	Damage Description
1	No Damage	No Damage
2	Hanger	20% Damage
3	Hanger	50% Damage
4	Hanger	Disconnected
5	Bridge Deck	4 cm Long Transverse Crack
6	Bridge Deck	8 cm Long Transverse Crack

3.2. Feasibility Analysis of Extracting Displacement Time-History Data at a Point Using Image Recognition Technology

3.2.1. Establishment of the Finite Element Model

The finite element analysis model was constructed using MIDAS/CIVIL 2021 software based on the bridge model. The ends of the main cables and the bottom of the bridge towers were fixed, the connection between the main cables and the bridge towers was rigid (with longitudinal constraints released), and the connections between the hangers and the bridge deck were also rigid. The entire bridge was discretized into 148 elements.

The established finite element model is shown in Figure 3. Loads were applied according to the conditions listed in Table 1.

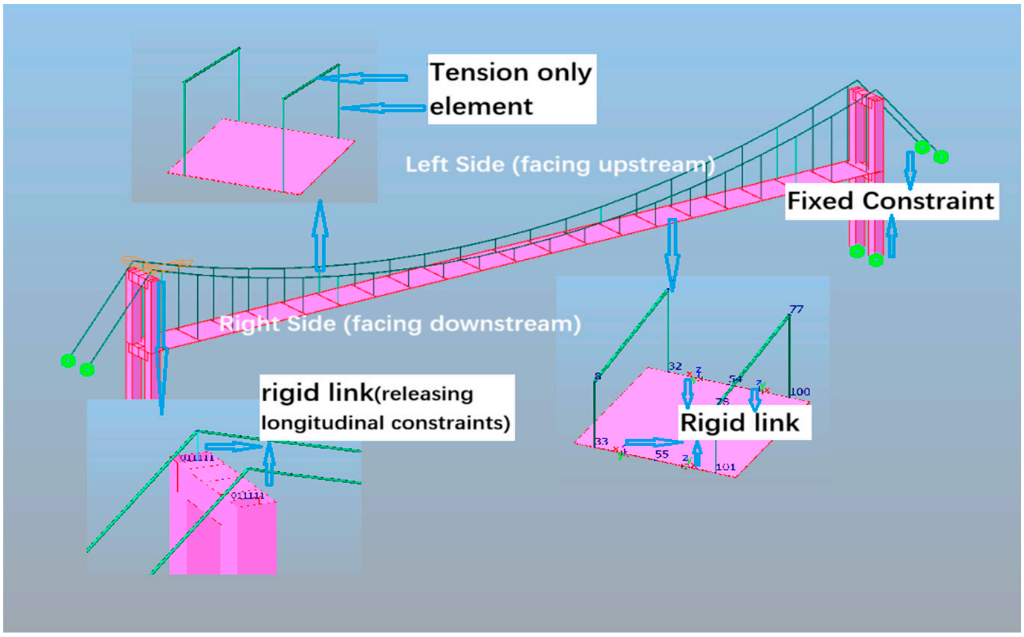

Figure 3. Finite Element Model of the Entire Bridge.

3.2.2. Capturing Structural Vibration Videos

A camera was used to capture the structural vibrations with an image magnification factor of 0.6 and a shooting distance of 4 m. The calculated pixel size in the video is approximately 6.8 mm. The moving load was simulated using an electric motor and a small vehicle to apply loads to the bridge. The vehicle's moving speed, motor rotation speed, and the centrifugal force generated by the motor could be adjusted, as shown in Figure 4. Specifically, a rotating hammer was fixed to the motor's drive shaft using screws and nuts, and the cosine load was simulated by the centrifugal force generated by the rotating hammer driven by the motor. The centrifugal force was adjusted by changing the length of the hammer's handle to alter the distance from the hammer to the drive shaft. The motor was fixed to the small vehicle, allowing the vehicle to move back and forth at a set speed while the motor operated, accompanied by the centrifugal force generated by the motor.

Figure 4. Moving Load Application Device.

3.2.3. Comparison of Displacement Time-History Data from Two Methods

The code for image recognition is provided in Supplementary Materials, Code S9, and the corresponding point numbers in the structure are shown in Figure 5. Two methods were used to analyze different load and damage conditions, as illustrated in Figure 6. The displacement time-history curves of the corresponding points in the structure were obtained and are summarized in Table 3.

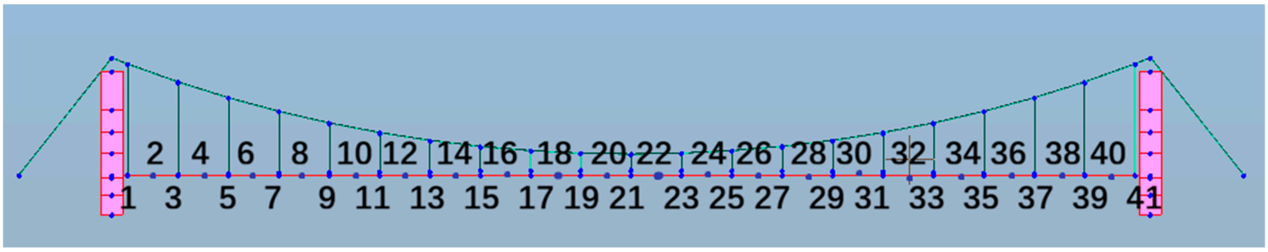

Figure 5. Point Number Location Diagram.

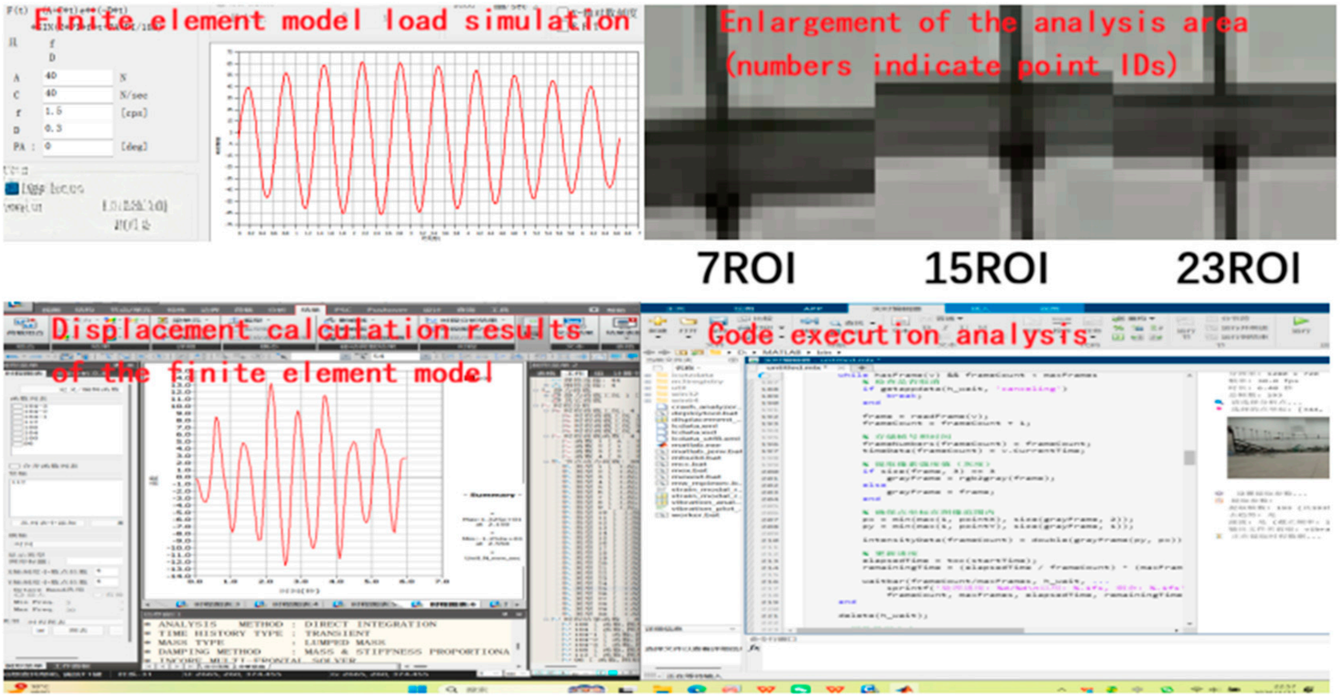

Figure 6. Finite Element and Image Recognition Analysis.

As shown in the figure, the displacement time-history curves obtained from finite element analysis and image recognition analysis are in good agreement. This indicates that extracting displacement time-history data of points through image recognition analysis is feasible.

Table 3. Comparison of Displacement Time-History Data.

<table>
<tr><th>Node ID</th><th>Load Condition</th><th>Damage Condition</th><th>Finite Element Analysis</th><th>Image Recognition Analysis</th></tr>
<tr><td>5</td><td>A</td><td>1</td><td>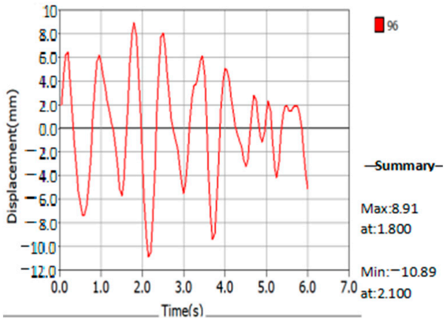
</td><td>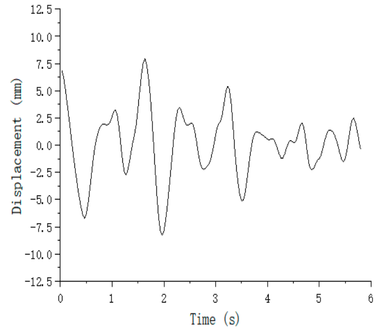
</td></tr>
<tr><td>13</td><td>A</td><td>2</td><td>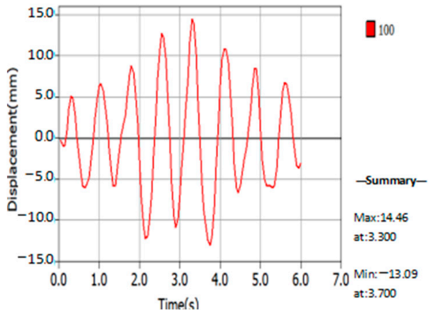
</td><td>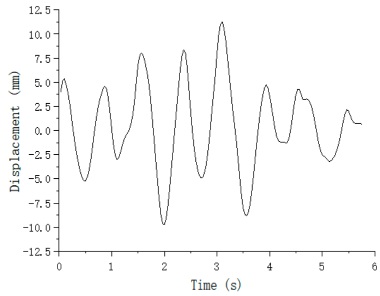
</td></tr>
<tr><td>23</td><td>A</td><td>1</td><td>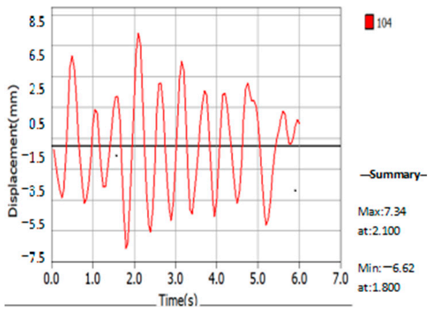
</td><td>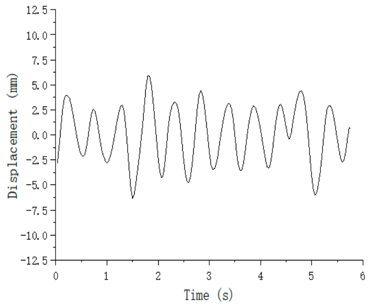
</td></tr>
<tr><td>23</td><td>B</td><td>1</td><td>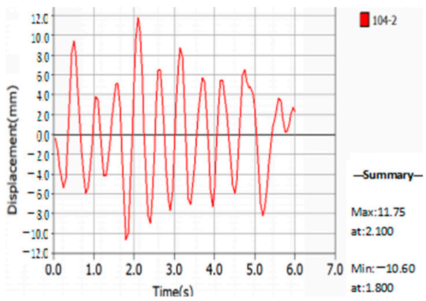
</td><td>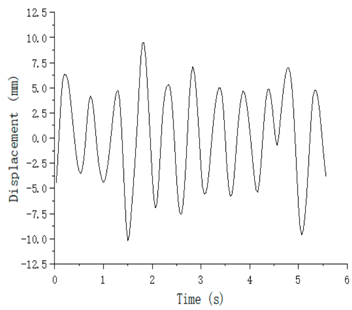
</td></tr>
</table>

3.3. Variation Patterns of Strain Mode Change Rate Under Structural Damage

Using the two methods, the first-order strain mode change rates of the hangers under different damage conditions were calculated, as shown in Table 4. The node locations remain the same as above.

Table 4. Variation Patterns of Strain Mode Change Rate.

1	Finite Element Analysis	Image Recognition Analysis
Hanger Damage	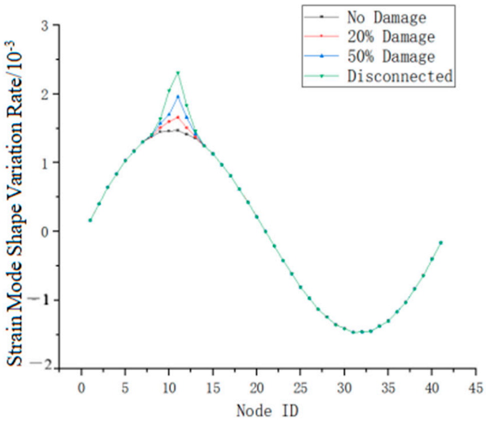	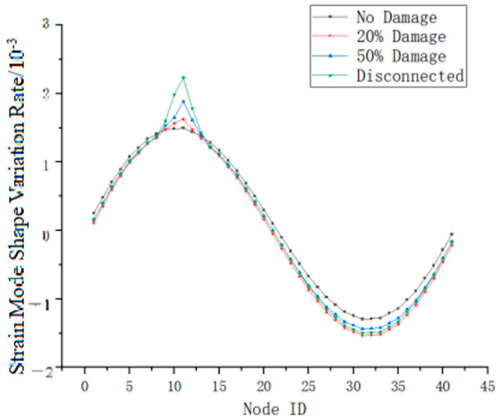
Bridge Deck Damage	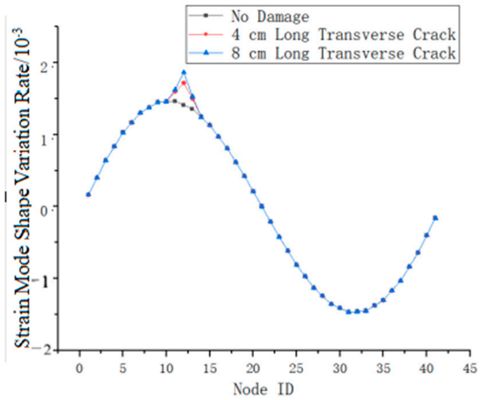	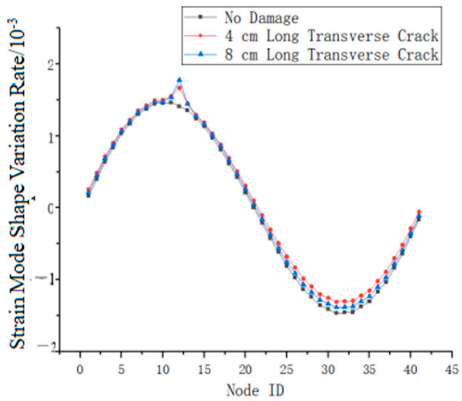

From the table, it can be observed that under undamaged conditions, the strain mode change rate shows no peak. When damage occurs, peaks appear at the corresponding locations in the strain mode change rate. In cases of varying degrees of hanger damage, the magnitude of the peak varies, with larger damage levels corresponding to higher peak values. Therefore, the degree of hanger damage can be assessed based on the peak magnitude. Similarly, for bridge deck cracks of different lengths, the peak magnitude also varies, with larger crack lengths corresponding to higher peaks. Hence, the length of bridge deck cracks can be evaluated based on the peak magnitude. Additionally, it is evident that hanger damage results in broader peak ranges, while bridge deck damage leads to narrower peak ranges. Thus, the type of damage can be identified based on the peak range, i.e., the number of nodes involved. The results from image recognition analysis align well with those from finite element analysis, demonstrating that image recognition technology can effectively locate structural damage and identify the type of damaged components.

3.4. Deviation Rate of Strain Mode Change Rate Under Structural Damage

Using the two methods, the deviation rates of the first-order strain mode change rates for the hangers under different damage conditions were calculated, as shown in Table 5. The node locations remain the same as above.

Table 5. Deviation Rate of Strain Mode Change Rate.

Damage Case	Finite Element Analysis			Image Recognition Analysis		
	Damaged	Undamaged	Deviation Rate of Strain Mode Change Rate	Damaged	Undamaged	Deviation Rate of Strain Mode Change Rate
2	1.66	1.47	12.9%	1.63	1.43	14.0%
3	1.95	1.47	33.2%	1.88	1.43	31.5%
4	2.31	1.47	57.1%	2.23	1.43	55.9%
5	1.72	1.47	17.0%	1.67	1.43	16.8%
6	1.87	1.47	27.2%	1.78	1.43	24.5%

From Table 5, it can be observed that when the hanger damage ranges from 20% to complete failure, the deviation rate of the strain mode change rate varies from 14.0% to 55.9%. When the crack length to bridge deck width ratio ranges from 1:10 to 1:20, the deviation rate of the strain mode change rate varies from 16.8% to 24.5%. The degree of damage in both hangers and the bridge deck corresponds to the deviation rate of the strain mode change rate, indicating that the damage severity can be evaluated based on the deviation rate. In practical engineering, since the strain mode change rate under healthy structural conditions is often unknown, a smooth curve fitted to the strain mode change rate curve under damaged conditions can be used to approximately calculate the deviation rate. The results from image recognition analysis align closely with those from finite element analysis, demonstrating that image recognition technology can effectively assess the degree of structural damage.

3.5. Summary

By analyzing displacement time-history data and strain mode change rates under different load and damage conditions using image recognition methods, and validating the results with finite element software, the following conclusions are drawn:

(1) Displacement time-history data at various points in a structure can be extracted using image recognition technology.
(2) No peaks appear in the strain mode change rate under undamaged structural conditions.
(3) When damage occurs, peaks appear at corresponding locations in the strain mode change rate.
(4) The severity of damage in hangers and bridge decks can be evaluated based on the magnitude of these peaks.
(5) The type of damage can be identified based on the range of the peaks, i.e., the number of nodes involved.
(6) The degree of damage corresponds to the deviation rate of the strain mode change rate, allowing damage severity to be evaluated quantitatively.
(7) In practical engineering, a smooth curve fitted to the strain mode change rate curve under damaged conditions can be used to approximately calculate the deviation rate.
(8) Damage identification can be achieved by analyzing the strain mode change rate and its deviation rate without requiring modal information from the bridge's healthy state.

4. Engineering Application

To validate the feasibility of the above conclusions and analysis methods, the stress of the bridge deck of an operational suspension bridge was tested and analyzed. The study aimed to determine whether damage exists, locate the damage, and assess its severity.

4.1. Testing Introduction

4.1.1. Bridge Structural Parameters

The suspension bridge has a span of 68 m and a deck width of 2 m. The main cable follows a parabolic profile, with a vertical distance of 6 m from the deck at the towers and 1.2 m at mid-span, resulting in a sag-to-span ratio of 1:14.583. The main cables are made of high-strength steel wires with a diameter of 30 mm and a spacing of 2.04 m. The hangers are Q235 steel rods with a diameter of 20 mm and a spacing of 2 m. The lower ends of the hangers are hinged to No. 10 channel steel crossbeams, which are welded to four equally spaced channel steel longitudinal beams. The deck consists of 4 mm thick patterned steel plates, each measuring 2 m $\times$ 2 m. The plates are bolted to the longitudinal beams and welded at the joints, as shown in Figure 7.

Figure 7. On-Site Photo of the Bridge.

4.1.2. Testing Introduction

A camera was used to capture the structural response with a magnification of 0.6$\times$ from a distance of 35 m. The testing was conducted on a windless, overcast day with stable temperatures, and the camera was securely fixed. The calculated pixel size in the video is approximately 35.7 mm. Video image analysis was performed on 69 points, including the hanger attachment points on the bridge deck and the midpoints between every two hangers.

4.1.3. Load Introduction

The primary traffic loads on the bridge consist of two-wheeled and three-wheeled motorcycles. Vibration videos of the bridge under moving loads were captured under four load cases:

Case 1: One three-wheeled motorcycle traveling in one direction.
Case 2: One two-wheeled motorcycle carrying one person traveling in one direction.
Case 3: One two-wheeled motorcycle carrying one person returning.
Case 4: Two two-wheeled motorcycles, each carrying two people, returning.

The load cases are illustrated in Figure 8.

https://doi.org/10.3390/app16052553

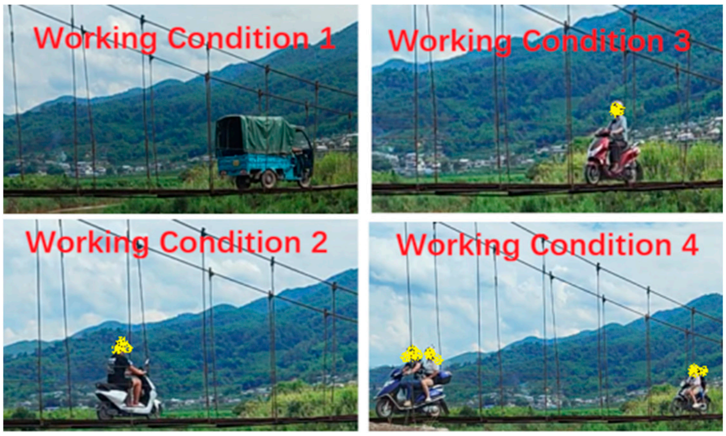

Figure 8. Load Case Diagram.

4.2. Testing Analysis

4.2.1. Extraction of Displacement Time-History Data

Displacement time-history data for 69 points on the bridge side were extracted under the four load cases. Table 6 presents the displacement time-history curves for points 50 and 55 under load cases 1 and 4, extracted via video image analysis.

Table 6. Displacement Time-History Curves.

Load Case	50	55
1	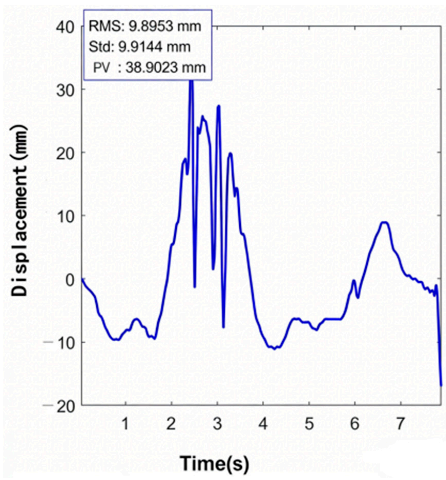	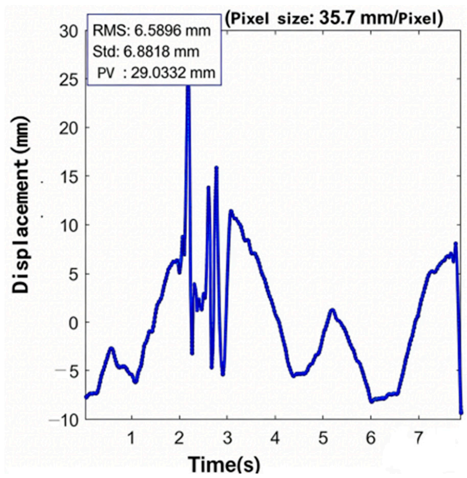
2	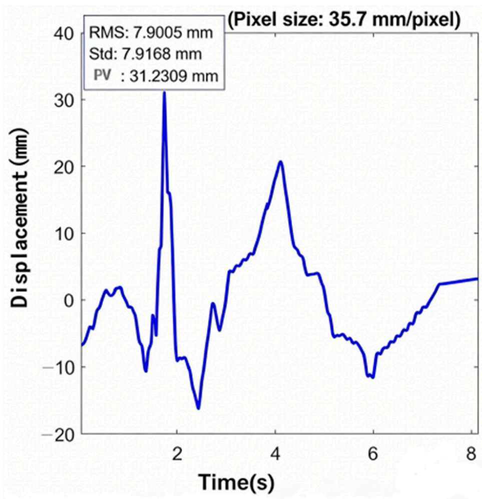	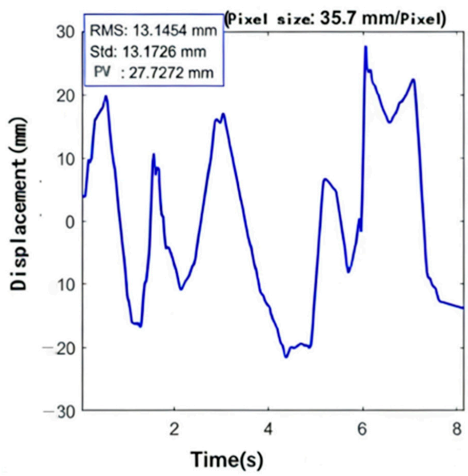

4.2.2. Strain Mode Change Rate Curve Analysis

The video images from the four on-site load cases were processed to obtain the strain mode change rates, as shown in Figure 9.

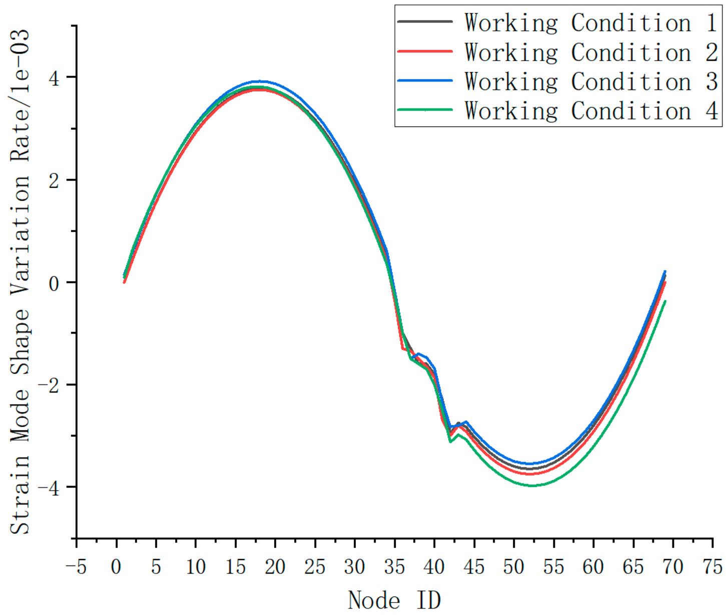

Figure 9. Strain Mode Change Rate Curves.

From Figure 9, it can be observed that under the four load cases, peaks appear in the strain mode change rate curves at points 37 and 42, indicating structural damage at these locations. The peak at point 37 covers a broader range, suggesting damage to the hanger at this point. The peak at point 42 is narrower, indicating a crack in the bridge deck near this measurement point.

4.2.3. Deviation Rate Analysis of Strain Mode Change Rate

A smooth curve was fitted to the strain mode change rate curve under damaged conditions to calculate the deviation rate, as illustrated in Figure 10. The calculation results are summarized in Table 7.

Table 7. Deviation Rate of Strain Mode Change Rate.

Point	Load Case	Measured Value	Fitted Value	Deviation Rate of Strain Mode Change Rate
37	1	−1.3	−1.12	16.07%
	2	−1.35	−1.15	17.39%
	3	−1.33	−1.13	17.70%
	4	−1.5	−1.28	17.19%
42	1	−2.97	−2.57	15.56%
	2	−2.81	−2.48	13.31%
	3	−2.83	−2.50	13.20%
	4	−3.12	−2.73	14.29%

Under the four load cases, Table 7 shows that the deviation rate at point 37 is approximately 17%. Based on previous calculations, it can be inferred that the stiffness loss of the hanger at point 37 is around 22%. The deviation rate at point 42 is approximately 14%, suggesting that the crack length at this location is about 1/8 of the transverse dimension of the bridge deck.

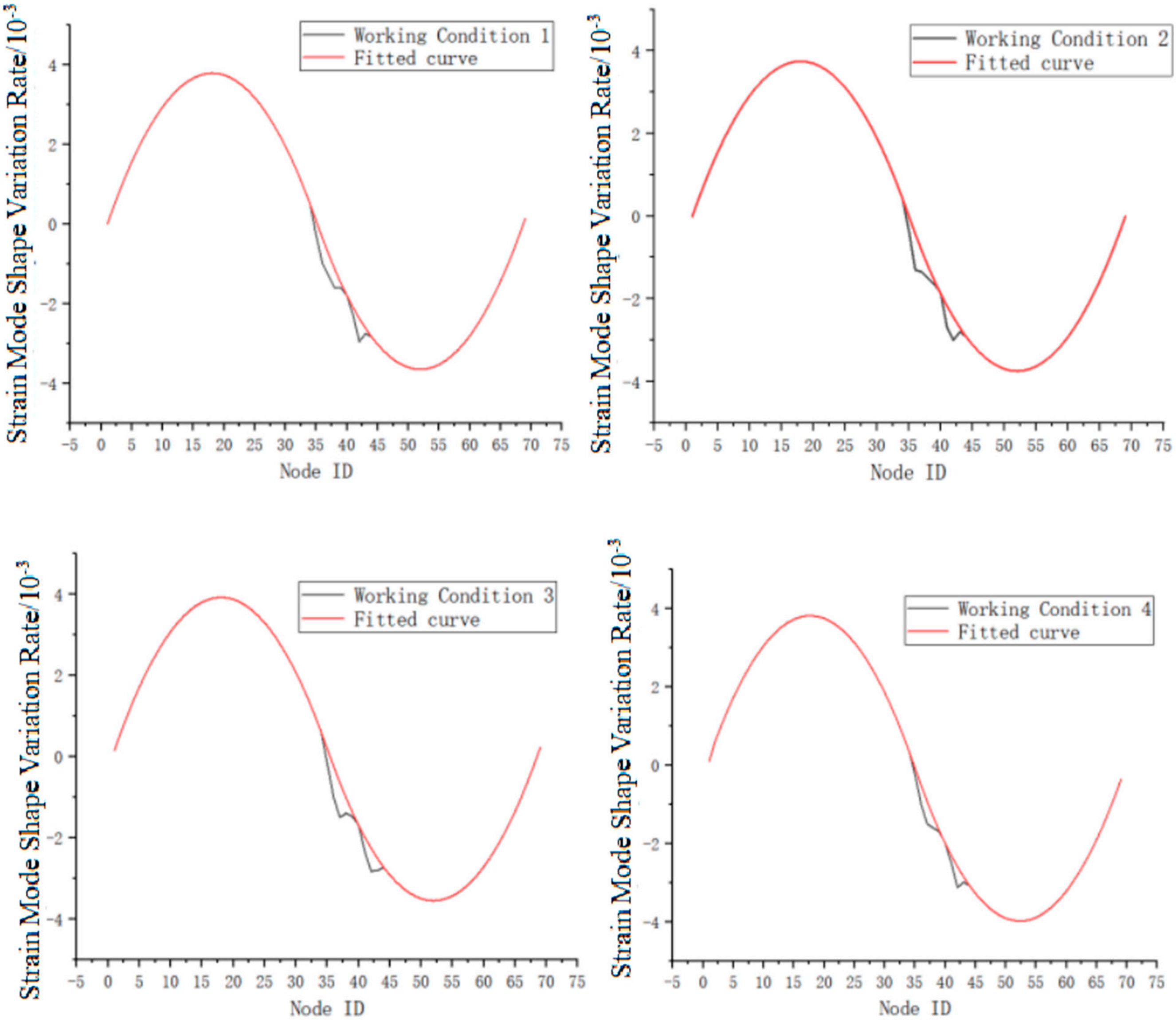

Figure 10. Fitted Strain Mode Change Rate Curve.

4.3. On-Site Inspection Verification and Conclusions

4.3.1. On-Site Inspection Analysis

Combined with the data analysis, an on-site inspection of the bridge was conducted. The inspection revealed that the hanger at point 37 consisted of two independent rods welded together and exhibited bending (as shown in Figure 11). This indicates that the hanger is subjected to both tension and bending during loading, resulting in reduced vertical stiffness within the suspension bridge system. As indicated by the theoretical analysis, a decrease in hanger stiffness affects the stress distribution in the bridge deck. Additionally, near point 42, a complete weld failure was found in the bridge deck, with a crack length of 6.1 cm. The total weld length was 51.4 cm, giving a crack length to total weld length ratio of approximately 1:8.43. This suggests that the crack in the bridge deck has reduced its stiffness, leading to increased stress in adjacent areas.

Figure 11. On-site Inspection Photos.

4.3.2. Conclusions

Based on the above findings and on-site measurements, the following conclusions can be drawn:

(1) Peaks in the strain mode change rate curves at points 37 and 42 indicated potential damage, which was confirmed by on-site inspection.
(2) The broad peak range at point 37 suggested hanger damage, while the narrow peak range at point 42 indicated a crack in the bridge deck. Both were validated by on-site inspection.
(3) The deviation rates of the strain mode change rate suggested approximately 22% stiffness loss in the hanger and a crack length ratio of about 1:8 relative to the bridge deck's transverse dimension, consistent with on-site inspection results.

5. Conclusions and Discussion on Limitations

Through theoretical derivation, finite element simulation, physical model experiments, and field validation on an actual bridge, the following conclusions are drawn:

(1) Displacement time-history data at various points in a structure can be extracted using image recognition technology. Compared to traditional methods, this approach avoids issues such as unstable data transmission, power interruptions, environmental interference, and limited measurement points, thereby improving data completeness and reliability. It enables effective identification and assessment of bridge damage.
(2) Under undamaged conditions, the strain mode change rate curve is smooth and peak-free. Peaks appear at corresponding locations when structural damage occurs.
(3) The range of peaks in the strain mode change rate curve, i.e., the number of nodes involved, can be used to identify the damaged component and the type of damage.
(4) The degree of damage corresponds to the deviation rate of the strain mode change rate, allowing quantitative assessment of damage severity.
(5) In practical engineering, a smooth curve fitted to the strain mode change rate curve under damaged conditions can be used to approximate the deviation rate.
(6) Damage identification can be achieved by analyzing the strain mode change rate and its deviation rate, without requiring modal information from the bridge's healthy state.

While the proposed visual image recognition method demonstrates promising results for suspension bridge damage identification, several limitations should be acknowledged to provide an objective perspective and guide future research:

(1) The accuracy of this method is inherently dependent on imaging conditions. The current implementation requires stable environmental conditions (e.g., windless weather, stable temperature) and a fixed camera setup. In practical field applications, factors such as ambient light variations, wind, and atmospheric disturbances may introduce measurement noise and affect the precision of pixel tracking.
(2) Spatial resolution constraints pose a challenge for detecting minor or incipient damage. At a shooting distance of 4 m with 1080 p resolution, the theoretical pixel size is approximately 6.8 mm. Although sub-pixel estimation techniques are employed, the sensitivity of this method to microscopic damage (e.g., early-stage fatigue cracks) remains to be thoroughly validated.
(3) The laboratory validation was conducted under controlled conditions with a simplified cosine excitation. Actual bridges are subjected to complex stochastic loads (e.g., traffic, wind, temperature effects) and operate in noisy environments. The performance of this method under such realistic conditions requires further investigation.
(4) This study focuses on a specific bridge type (suspension bridge) and damage scenarios (hanger damage and plate fracture). The generalizability of this method to other bridge types (e.g., cable-stayed bridges, arch bridges, girder bridges) remains to be verified.

Future work will address these limitations by exploring adaptive camera stabilization techniques, higher-resolution imaging systems, advanced denoising algorithms, and field validation on in-service bridges.

Supplementary Materials: The following supporting information can be downloaded at https://www.mdpi.com/article/10.3390/app16052553/s1: Computational Code. Code S1: MATLAB script for reading video frames sequentially using the VideoReader function. (Video_Reading.m); Code S2: MATLAB script implementing the Phase Correlation Method for high-precision pixel tracking and displacement calculation between video frames. (Pixel_Tracking_PCM.m); Code S3: MATLAB script for generating the displacement time-history curve of a tracked point from the frame-by-frame translation data. (Displacement_TimeHistory.m); Code S4: MATLAB script for constructing the Hankel matrix from multi-point displacement time-history data. (Build_Hankel_Matrix.m); Code S5: MATLAB script for performing Singular Value Decomposition (SVD) on the Hankel matrix to determine system order. (SVD_Decomposition.m); Code S6: MATLAB script for extracting the discrete-time state-space system matrices (Ad, C) from the SVD results and time-shifted Hankel matrix. (Extract_System_Matrices.m); Code S7: MATLAB script for modal parameter identification, including eigenvalue decomposition, conversion to continuous-time domain, and calculation of natural frequencies, damping ratios, and displacement mode shapes. (Modal_Parameter_ID.m); Code S8: MATLAB script for calculating strain mode shapes from displacement mode shapes using a central difference approximation of the spatial second derivative. (StrainMode_From_DisplacementMode.m). Code S9: Complete Computational Code for Extracting Displacement, Velocity, Acceleration Time-History Data, Spectral Analysis Data, and Phase Diagram Data from a Point Based on Video Images. Code S10: Complete Computational Code for Extracting Structural Mode Shape Analysis, Strain Modal Analysis, and Other Data Based on Video Images (Using 19 Points as an Example).

Author Contributions: Data curation, X.L.; Writing—original draft, X.L.; Project administration, K.M.; Funding acquisition, K.M. All authors have read and agreed to the published version of the manuscript.

Funding: This research received no external funding.

Institutional Review Board Statement: Not applicable. This study did not involve human participants, animal subjects, or any personal data requiring ethical review. The research exclusively utilized publicly available video images of bridge structures and numerical simulations based on publicly accessible data.

Informed Consent Statement: Not applicable. This study did not involve human subjects, and all data used were obtained from publicly available sources or generated through computational methods.

Data Availability Statement: The data supporting the findings of this study are available within the article and its Supplementary Materials. All relevant datasets, simulation codes, and analytical results are included as part of the submitted manuscript files for review and reproducibility purposes.

Conflicts of Interest: The authors declare no conflicts of interest.

References

1. Bridge Science Research Institute of Railway Ministry Bridge Engineering Bureau (Ed.) *Suspension Bridges*; Science and Technology Documentation Press: Beijing, China, 1996.
2. Qiao, H.; Guan, H.; Zhu, Y. Footbridge structural health monitoring—A review of current research and future directions. *Struct. Infrastruct. Eng.* **2025**, *21*, 1–24. [CrossRef]
3. An, Y.; Chatzi, E.; Sim, S.H.; Laflamme, S.; Blachowski, B.; Ou, J. Recent progress and future trends on damage identification methods for bridge structures. *Struct. Control Health Monit.* **2019**, *26*, e2416. [CrossRef]
4. Cui, C.; Chen, A.; Ma, R. An improved continuum damage mechanics model for evaluating corrosion-fatigue life of high-strength steel wires in the real service environment. *Int. J. Fatigue* **2020**, *135*, 105540. [CrossRef]
5. Mehrabi, A.B. In-service evaluation of cable-stayed bridges, overview of available methods and findings. *J. Bridge Eng.* **2006**, *11*, 716–724. [CrossRef]
6. Xu, T.; Ma, J.; Wei, G.; Gong, B.; Liu, J. A Framework for Evaluating the Reasonable Internal Force State of the Cable-Stayed Bridge Without Backstays. *Buildings* **2024**, *14*, 3656. [CrossRef]
7. Wheeler, B.J.; Karimi, H.A. Deep Learning-Enabled Semantic Inference of Individual Building Damage Magnitude from Satellite Images. *Algorithms* **2020**, *13*, 195. [CrossRef]
8. Xu, J.; Wang, H.; Cui, C.; Zhao, B.; Li, B. Oil Spill Monitoring of Shipborne Radar Image Features Using SVM and Local Adaptive Threshold. *Algorithms* **2020**, *13*, 69. [CrossRef]
9. Xin, J.; Zhou, J.; Yang, S.X.; Li, X.; Wang, Y. Bridge Structure Deformation Prediction Based on GNSS Data Using Kalman-ARIMA-GARCH Model. *Sensors* **2018**, *18*, 298. [CrossRef]
10. Tang, Q.; Zhou, J.; Xin, J.; Zhao, S.; Zhou, Y. Autoregressive Model-Based Structural Damage Identification and Localization Using Convolutional Neural Networks. *KSCE J. Civ. Eng.* **2020**, *24*, 2173–2185. [CrossRef]
11. Kim, Y.; Chong, J.W.; Chon, K.H.; Kim, J. Wavelet-based AR–SVM for health monitoring of smart structures. *Smart Mater. Struct.* **2012**, *22*, 015003. [CrossRef]
12. de Lautour, O.R.; Omenzetter, P. Damage classification and estimation in experimental structures using time series analysis and pattern recognition. *Mech. Syst. Signal. Process.* **2010**, *24*, 1556–1569. [CrossRef]
13. Lei, J.Q.; Zheng, M.Z.; Xu, G.Y. *Design of Suspension Bridges*; China Communications Press: Beijing, China, 2002.
14. Casciati, S.; Elia, L. Damage localization in a cable-stayed bridge via bio-inspired metaheuristic tools. *Struct. Control Health Monit.* **2016**, *23*, e2710. [CrossRef]
15. Guzman-Acevedo, G.M.; Quintana-Rodriguez, J.A.; Vazquez-Becerra, G.E.; Martinez-Trujano, L.A.; Carrion-Viramontes, F.J.; Garcia-Armenta, J. Tension Force Estimation of Cable-Stayed Bridges Based on Computer Vision Without the Need for Direct Measurement of Mechanical Parameters of the Cables. *Sensors* **2025**, *25*, 3910. [CrossRef]
16. Jin, P.; Zhao, Z. Research on cable force monitoring of large-span cable-stayed bridge based on Internet of Things technology. In Proceedings of the Sensing, Measurement, Communication and IoT Technologies Conference, Luoyang, China, 28–30 November 2025.
17. Ma, S.; Yan, W.; Huang, Y.; Jiang, J.; Hu, S.; Wang, Y. Calibration method of low-light sensor based on bridge lights. *J. Atmos. Ocean. Technol.* **2016**, *33*, 1123–1134. [CrossRef]
18. Chen, G.; Ren, W. Identification of Fundamental Frequency of Cables in Cable-Stayed Bridges Based on Ambient Vibration. *Earthq. Eng. Eng. Vib.* **2003**, *23*, 100–106. [CrossRef]
19. Civera, M.; Sibille, L.; Fragonara, L.Z.; Ceravolo, R. A DBSCAN-based automated operational modal analysis algorithm for bridge monitoring. *Measurement* **2023**, *208*, 112451. [CrossRef]
20. Fang, Z.; Wang, J.Q. Practical formula for cable tension estimation by vibration method. *J. Bridge Eng.* **2012**, *17*, 161–164. [CrossRef]
21. Li, Y.Q.; Zhao, H.W.; Yue, Z.X.; Li, Y.W.; Zhang, Y.; Zhao, D.C. Real-time intelligent prediction method of cable's fundamental frequency for intelligent maintenance of cable-stayed bridges. *Sustainability* **2023**, *15*, 4086. [CrossRef]
22. Lu, N.; Zeng, W.; Cui, J.; Luo, Y.; Liu, X.; Liu, Y. An Advanced Computer Vision Method for Noncontact Vibration Measurement of Cables in Cable-Stayed Bridges. *Struct. Control Health Monit.* **2025**, *2025*, 1254049. [CrossRef]
23. Meng, F.; Yu, J.; Alaluf, D.; Mokrani, B.; Preumont, A. Modal flexibility based damage detection for suspension bridge hangers: A numerical and experimental investigation. *Smart Struct. Syst.* **2019**, *23*, 15–29. [CrossRef]

24. Guan, D.; Li, J.; Chen, J. Optimization Method of Wavelet Neural Network for Suspension Bridge Damage Identification. In Proceedings of the 2016 2nd International Conference on Artificial Intelligence and Industrial Engineering (AIIE 2016), Beijing, China, 20–21 November 2016.
25. Seyedpoor, S.M.; Nopour, M.H. A two-step method for damage identification in moment frame connections using support vector machine and differential evolution algorithm. *Appl. Soft Comput.* **2020**, *88*, 106008. [CrossRef]
26. Fan, C.; Zheng, Y.; Wang, B.; Zhou, Y.; Sun, M. Damage identification method for tied arch bridge suspender based on quasi-static displacement influence line. *Mech. Syst. Signal Process.* **2023**, *200*, 110518. [CrossRef]
27. Sundravel, K.; Vijaya, R.; Jagadeesan, A.; Dhanush, A.; Sanjay Kumar, A. A Review of Innovations, Challenges, and Future Directions in Structural Health Monitoring Using Smart Materials. *J. Environ. Nanotechnol.* **2025**, *14*, 464–478. [CrossRef]
28. Mengesha, G. Integrating AI in structural health monitoring (SHM): A Systematic Review on Advances, Challenges, and Future Directions. *I-Manag. J. Struct. Eng.* **2024**, *13*, 43–58. [CrossRef]
29. Zhang, H.; Li, H.; Zhou, J.; Tong, K.; Xia, R. A multi-dimensional evaluation of wire breakage in bridge cable based on self-magnetic flux leakage signals. *J. Magn. Magn. Mater.* **2023**, *566*, 170321. [CrossRef]
30. Duan, H.; Liu, H.; Sun, Y.; Gao, H. Determination of reasonable internal force state for cable-stayed bridge without backstays. *J. Civ. Struct. Health Monit.* **2023**, *13*, 1243–1263. [CrossRef]
31. Chen, G.; Shi, W.; Yu, L.; Huang, J.; Wei, J.; Wang, J. Wireless Sensor Placement Optimization for Bridge Health Monitoring: A Critical Review. *Buildings* **2024**, *14*, 856. [CrossRef]
32. Machelski, C.; Hildebrand, M.; Rybak, J. Measurement of deformation and force changes recorded during long-term monitoring of a steel cable-stayed bridge. *Sensors* **2025**, *25*, 3638. [CrossRef] [PubMed]
33. Kong, X.; Liu, Z.; Liu, H.; Hu, J.; Deng, L. Recent advances on inspection, monitoring, and assessment of bridge cables. *Eng. Struct.* **2024**, *310*, 116227. [CrossRef]
34. Liu, X.; Yang, J.; Zhuo, W.; Lin, Y. Real-time identification of time-varying cable force for cable-stayed bridges based on vibration monitoring. *Measurement* **2024**, *214*, 112497. [CrossRef]
35. Xu, W.; Zhu, W.; Su, Z.; Cao, M.; Xu, H. A novel structural damage identification approach using damage-induced perturbation in longitudinal vibration. *J. Sound Vib.* **2021**, *496*, 115932. [CrossRef]
36. Zui, H.; Shinke, T.; Namita, Y. Practical formulas for estimation of cable tension by vibration method. *J. Struct. Eng.* **1996**, *122*, 651–656. [CrossRef]
37. Hoang, H.; Hoang, V.; Nguyen, D. Long-term monitoring of cable tension force in cable-stayed bridges using vibration-based method: Case of Binh Bridge. *Eng. Technol. Appl. Sci. Res.* **2025**, *15*, 20300–20313. [CrossRef]
38. Liu, Z.; Guo, T.; Han, D.; Li, A. Experimental study on corrosion-fretting fatigue behavior of bridge cable wires. *J. Bridge Eng.* **2020**, *25*, 04020104. [CrossRef]
39. Wang, L.; Xiao, Z.; Duan, C.; Li, W.; Fu, N. Research on Algorithm of Corrosion Fatigue Damage Evolution of Stay Cables and Structural Mechanical Behavior with Cable Fracture. *Appl. Sci.* **2023**, *13*, 4890. [CrossRef]
40. Li, D.; Li, B.; Wang, T.; Zhang, J. Lightweight structural health monitoring and safety evaluation. *Adv. Struct. Eng.* **2025**, *28*, 13694332251325043. [CrossRef]
41. Li, H.; Ou, J. The state of the art in structural health monitoring of cable-stayed bridges. *J. Civ. Struct. Health Monit.* **2016**, *6*, 43–67. [CrossRef]
42. Numan, M. Advancements in structural health monitoring: A review of machine learning approaches for damage detection and assessment. *Int. J. Comput. Civ. Struct. Eng.* **2024**, *20*, 124–142. [CrossRef]
43. CCCC Highway Consultants Co., Ltd. *JTG D60-2015 General Code for Design of Highway Bridges and Culverts*; China Communications Press: Beijing, China, 2015.
44. Alamdari, M.M.; Dang Khoa, N.L.; Wang, Y.; Samali, B.; Zhu, X. A multi-way data analysis approach for structural health monitoring of a cable-stayed bridge. *Struct. Health Monit.* **2018**, *18*, 35–48. [CrossRef]
45. He, Y.; Song, J.Z.; Yang, X.X. Comparative study on wind resistance performance of bridge towers in self-supporting state. *Struct. Eng.* **2007**, *23*, 49–55. Available online: https://wap.cnki.net/touch/web/Journal/Article/JGGC200706012.html (accessed on 25 February 2026).
46. Jiang, C.; Wu, C.; Cai, C.S.; Jiang, X.; Xiong, W. Corrosion fatigue analysis of stay cables under combined loads of random traffic and wind. *Eng. Struct.* **2020**, *206*, 110153. [CrossRef]
47. He, M.; Liang, P.; Wang, Y.; Xia, Z.; Wu, X. Online automatic monitoring of abnormal vibration of stay cables based on acceleration data from structural health monitoring. *Measurement* **2022**, *195*, 111102. [CrossRef]
48. Yang, Y. Research progress on calibration of bridge structural health monitoring sensors. *Adv. Bridge Eng.* **2024**, *5*, 32. [CrossRef]
49. Zhang, K.; Shen, X.; Bao, L.; Liu, H. Process monitoring and terminal verification of cable-stayed bridges with corrugated steel webs under construction. *Struct. Durab. Health Monit.* **2023**, *17*, 131–158. [CrossRef]
50. Ye, H.; Duan, Z.; Tang, S.; Yang, Z.; Xu, X. Fatigue crack growth and interaction of bridge wire with multiple surface cracks. *Eng. Fail. Anal.* **2020**, *116*, 104739. [CrossRef]

51. Gonzalez, R.C.; Woods, R.E. *Digital Image Processing*, 4th ed.; Pearson: New York, NY, USA, 2018.
52. Fleet, D.J.; Jepson, A.D. Computation of component image velocity from local phase information. *Int. J. Comput. Vis.* **1990**, *5*, 77–104. [CrossRef]
53. Szeliski, R. *Computer Vision: Algorithms and Applications*, 2nd ed.; Springer: London, UK, 2022.
54. Bracewell, R.N. *The Fourier Transform and Its Applications*, 3rd ed.; McGraw-Hill: New York, NY, USA, 2000.
55. Kuglin, C.D.; Hines, D.C. The phase correlation image alignment method. In *Proceedings of the IEEE International Conference on Cybernetics and Society, San Francisco, CA, USA, 23–25 September 1975*; IEEE: Piscataway, NJ, USA, 1975; pp. 163–165.
56. Reddy, B.S.; Chatterji, B.N. An FFT-based technique for translation, rotation, and scale-invariant image registration. *IEEE Trans. Image Process.* **1996**, *5*, 1266–1271. [CrossRef]
57. Juang, J.N.; Pappa, R.S. An eigensystem realization algorithm for modal parameter identification and model reduction. *J. Guid. Control Dyn.* **1985**, *8*, 620–627. [CrossRef]
58. Overschee, P.V.; Moor, B.D. *Subspace Identification for Linear Systems: Theory, Implementation, Applications*; Springer: Boston, MA, USA, 1996.
59. Golub, G.H.; Van Loan, C.F. *Matrix Computations*, 4th ed.; Johns Hopkins University Press: Baltimore, MD, USA, 2013.
60. Juang, J.N. *Applied System Identification*; Prentice Hall: Englewood Cliffs, NJ, USA, 1994.
61. Peeters, B.; De Roeck, G. Stochastic system identification for operational modal analysis: A review. *J. Dyn. Syst. Meas. Control* **2001**, *123*, 659–667. [CrossRef]
62. Ewins, D.J. *Modal Testing: Theory, Practice and Application*, 2nd ed.; Research Studies Press: Baldock, UK, 2000.
63. Maia, N.M.M.; Silva, J.M.M. *Theoretical and Experimental Modal Analysis*; Research Studies Press: Taunton, UK, 1997.
64. Pandey, A.K.; Biswas, M.; Samman, M.M. Damage detection from changes in curvature mode shapes. *J. Sound Vib.* **1991**, *145*, 321–332. [CrossRef]
65. Chance, J.; Tomlinson, G.R.; Worden, K. A simplified approach to the numerical and experimental modelling of the dynamics of a cracked beam. In *Proceedings of the 12th International Modal Analysis Conference, Honolulu, HI, USA, 31 January–3 February 1994*; Society for Experimental Mechanics, Inc.: Bethel, CT, USA, 1994; pp. 778–785.
66. Abdo, M.A.B.; Hori, M. A numerical study of structural damage detection using changes in the rotation of mode shapes. *J. Sound Vib.* **2002**, *251*, 227–239. [CrossRef]